

Design and Optimizations of a High-throughput Valve-based Microfluidic Device for Single Cell Compartmentalization and Analysis

Jonathan Briones

Osaka University

Wilfred Espulgar

Osaka University

Shohei Koyama

Osaka University

Hyota Takamatsu

Osaka University

Eiichi Tamiya

Osaka University

Masato Saito (✉ saitomasato@ap.eng.osaka-u.ac.jp)

Graduate School of Engineering, Osaka University, Suita, Osaka 565-0871, Japan

Research Article

Keywords: single cell screening platforms, genomics and proteomics, heterogeneity, drug discovery

Posted Date: December 11th, 2020

DOI: <https://doi.org/10.21203/rs.3.rs-119917/v1>

License: © ⓘ This work is licensed under a Creative Commons Attribution 4.0 International License.

[Read Full License](#)

Design and optimizations of a high-throughput valve-based microfluidic device for single cell compartmentalization and analysis

Jonathan Briones¹, Wilfred Espulgar¹, Shohei Koyama², Hyota Takamatsu², Eiichi Tamiya^{3,4}, and Masato Saito^{1,3*}

¹ Graduate School of Engineering, Osaka University, Suita, Osaka 565-0871, Japan

² Graduate School of Medicine, Osaka University, Suita, Osaka 565-0871, Japan

³ AIST PhotoBIO-OIL, Osaka University, Suita, Osaka 565-0871, Japan

⁴ The Institute of Scientific and Industrial Research, Osaka University, Suita, Osaka 565-0871, Japan

*correspondence: saitomasato@ap.eng.osaka-u.ac.jp

ABSTRACT

The need for high throughput single cell screening platforms has been increasing with advancements in genomics and proteomics to identify heterogeneity, unique cell subsets or super mutants from thousands of cells within a population. For real-time monitoring of enzyme kinetics and protein expression profiling, valve-based microfluidics or pneumatic valving that can compartmentalize single cells is advantageous by providing on-demand fluid exchange capability for several steps in assay protocol and on-chip culturing. However, this technique is throughput limited by the number of compartments in the array. Thus, one big challenge lies in increasing the number of microvalves to several thousand that can be actuated in the microfluidic device to confine enzymes and substrates in picoliter volumes. This work explores the design and optimizations done on a microfluidic platform to achieve high-throughput single cell compartmentalization as applied to single-cell enzymatic assay for protein expression quantification. Design modeling through COMSOL Multiphysics was utilized to determine the circular microvalve's optimized parameters, which can close thousands of microchambers in an array at lower sealing pressure. Multiphysical modeling results demonstrated the relationships of geometry, valve dimensions, and sealing pressure, which were applied in the fabrication of a microfluidic device comprising of up to 5000 hydrodynamic traps and corresponding microvalves. Comparing the effects of geometry, actuation media and fabrication technique, a sealing pressure as low as 0.04 MPa was achieved. Applying to single cell enzymatic assay, variations in granzyme B activity in Jurkat and human PBMC cells were observed. Improvement in the microfluidic chip's throughput is significant in single cell analysis applications, especially in drug discovery and treatment personalization.

Introduction

Microfluidic technology has become a popular choice for micro-total analysis systems as it provides high precision of liquid manipulation that conventional bench-top approaches are unable to do^{1,2}. Many research works have demonstrated its advantages in having fast isolation speed and high efficiency of data acquisition. It is capable of integrating multiple workflows that enables parallelization and streamlining of complex protocols, which allows automation and control of analytical functions, cell and cell environment manipulation, and simultaneous detection and quantification of secreted molecules^{3,4}. For instance, conventional approaches don't take into account the phenotypic and functional state of heterogeneous cells which microfluidics technology is able to address. Microfluidics' approach allows the identification of rare subsets and resolution between cells with same expression patterns. This makes microfluidic platforms an important tool for single cell studies.

There are several microfluidics techniques that can be utilized for single cell research like droplet microfluidics, optofluidics and optical trapping, microwells and hydrodynamic trapping, etc. In enzymatic activity assay that aims to quantify extracellular protein secretions (i.e. granzyme B) from each cell, a platform that is capable of compartmentalization, on-demand media exchanges for washing and reagent introduction, and real-time monitoring is needed. Here, a microvalve-based device is a better choice as compared to other techniques^{5,6}. There are several types of actuation mechanisms for microvalves, however this work focused on normally open pneumatic valves (i.e. Quake valves). A valve is made of a control channel that overlaps a flow channel and is separated by a thin membrane. Generally made of polydimethylsiloxane (PDMS), an external gas or liquid source that is connected to the control line provides pressure that actuates the valves, which cause the thin

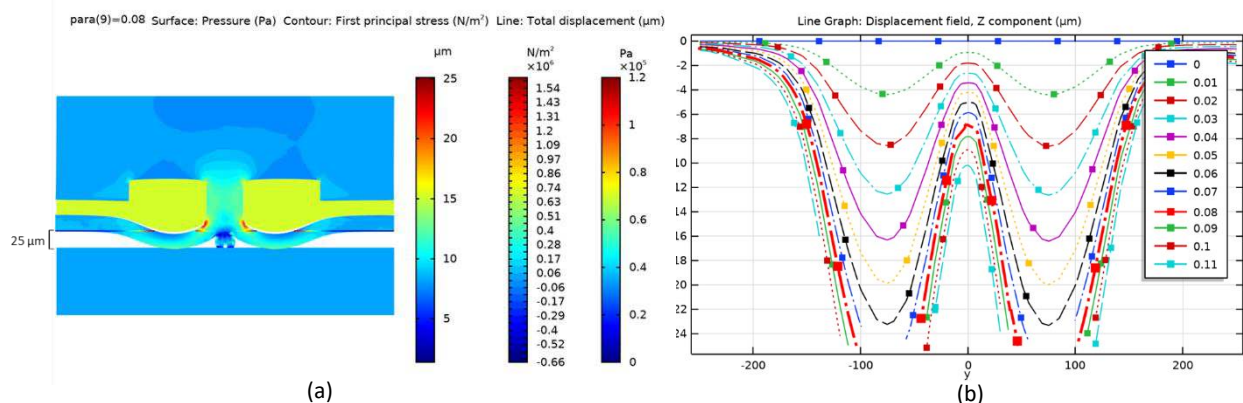


Figure 1. Multiphysics simulation of the unit valve's ($R=140 \mu\text{m}$, $h=50$) actuation. (a) 2D plot of the middle cut plane indicating membrane deflection, resulting surface pressure and first principal stress (b) line graph of the displacement field at various applied pressure (MPa) across the arc length.

membrane to deflect and block or close the flow channel^{6,7}. Nonetheless, the throughput of this technique is limited by the number of available compartments that can be sealed by actuated valves below critical pressure.

Meier et al. made use of 540 microfluidic PDMS membrane valves and Armbrrecht et al. used 1026 circular membrane valves and corresponding microchambers in their respective research works^{8,9}. Both works applied about 0.20 MPa as actuation pressure to seal the microchambers and isolate the samples. The group of Kellogg et al. applied ≈ 0.17 MPa (25 psi) in their control line to isolate single cells in 96 chambers¹⁰. Tong et al. needed ≈ 0.14 MPa (20 psi) to switch the valves (4 x 4 addressable ports) to a closed state¹¹.

With the advancements in the fabrication techniques of microchip-based screening devices, which are capable of nanoliter-scale liquid-handling, the throughput of single cell experiments also increases. High throughput screening has been defined as the analysis of more than 10^3 data points tested in parallel or very rapidly in succession^{12,13}. For a valve-based microfluidic device, increasing the number of chambers that can compartmentalize each cell to more than 10^3 is advantageous as it would allow greater representation of the sample population under investigation, which can further probe the significance of heterogeneities. However, this increase would also require design modifications and increased pressure to actuate all pneumatic valves and seal microchambers. An increase that can have negative effect on cell function and viability. Increasing the applied pressure, on the other hand, also put the thin PDMS membrane at risk of rupturing or breaking of the bonds between the polymer layers.

In this work, we sought to increase the number of microchambers in an array of a microfluidic chip that can be opened or closed with circular pneumatic valves. Using COMSOL Multiphysics, we looked into the effect of the geometry and dimensions of the valve design to the sealing pressure. The analysis of the multiphysics system model aims to reduce the value of the sealing pressure in real applications. These results were used to fabricate a microfluidic device with up to 5000 hydrodynamic traps and control microvalves via photolithography and soft lithography techniques. The effects of different actuation media and fabrication technique was also investigated to determine the lowest achievable sealing pressure within the constraints of the chip. The said device was later applied to perform a high-throughput single cell enzyme activity assay to profile the granzyme B (GrB) expression of each immune cell.

Results and Discussion

Model Implementation and valve design optimization. Figure 1 shows one of the simulations done on the microvalve unit. This 2D plot result of the middle cut plane models the valve actuation and the field displacement (z component) when a pressure of 0.08 MPa was applied to deflect the elastomer membrane across the flow channel with a height of $25 \mu\text{m}$. This example was chosen to show how the sealing pressure was determined during actuation to cause the membrane to be displaced to more than the flow channel's height.

The effect of the outer radius (R) of the circular valve model, the height (h), and the applied pressure, to the membrane displacement was compared and is summarized in figure 5. The modeling showed that with a valve height is $25 \mu\text{m}$, a valve radius of $80 \mu\text{m}$ requires a pressure of 0.33 MPa to deflect the membrane and create a sealed chamber. Increasing R to $100 \mu\text{m}$ decreases the sealing pressure to 0.21 MPa. Meanwhile an R of $120 \mu\text{m}$ needs to reach 0.13 MPa. Further increasing R to $140 \mu\text{m}$ lowers the sealing pressure to 0.08 MPa. When the valve height was increased to $50 \mu\text{m}$, a decrease in sealing pressure was computed. A sealing pressure of 0.29 MPa, 0.19 MPa, 0.12 MPa, and 0.075 MPa resulted from an R of $80 \mu\text{m}$, $100 \mu\text{m}$, $120 \mu\text{m}$, and $140 \mu\text{m}$, respectively.

It can be seen in figures 1 & 2 that, the displacement, for different loads, and the corresponding sealing pressure varies with R. Curve fitting by nonlinear regression (second order polynomial) shows a good fit with an R-square of 0.9999 (99.99%) for h1 and 1 (100%) for h2. It can also be seen that a higher h (h1 vs h2) resulted to a lower sealing pressure, although this difference decreases as the R increases.

From these results, we fabricated a microfluidic chip with arrays of microvalves with height of h2 (50 μ m), and R of 120 μ m and 140 μ m. One control line inlet is connected to about 750 circular valves. There are 3 interconnected inlets on each side of the device. We tested the actuation of these valves by applying air pressure at the control inlet. The flow layer was filled with a FITC dextran fluorescent solution and the fluorescence intensities were measured with and without actuation. A sealed chamber is determined when the intensity in the valve area is the same as the background or no fluorescent solution.

As shown in figure 2, the microfluidic valves with R of 120 μ m can be sealed with the lowest pressure of 0.13 MPa (mean, \bar{x} = 0.14 MPa, std. dev. = 0.011) as compared to the computational value of 0.12 MPa. On the other hand, experimental results for the valves with R=140 μ m showed a sealing pressure of 0.07 MPa (\bar{x} = 0.08 MPa, std.dev.=0.007) as compared to the simulation value of 0.075 MPa. The R was limited to a maximum value of 140 μ m as further increasing it would result to a greater separation distance between hydrodynamic traps, which lowers the trap occupancy rate, and increases overall microfluidic chip size.

We also compared the effect of different valve structures to the sealing pressure and the point of computation failure (rupture pressure), shown in figure 3. Valve structures A and B (Fig. 3a) both have a height of 50 μ m and lower radius R_v . However, structure B's upper radius R_u is smaller by 20 μ m, creating a step or bell like figure. The smaller top structure was chosen with the aim of reducing the material strain in the membrane as well as lower the total volume of the valve. This aspect ratio of smaller top and bigger bottom is also assumed to avoid membrane collapse.

Results showed that both valve structures A and B achieved the same sealing pressure at different R (Fig. 3b). However, when it comes to the maximum pressure that the unit can hold before failure, structure B reaches a higher value. This shows that structure A reaches a mode of failure first as the load increases. One difference among the two designs is the total volume of the valve unit, smaller for B. Figure 3c and 6d shows the von Mises stress of the solid at a cut line defined at the circular valve geometry of structures 3A and 3B, respectively. Structure 3B (fails at 0.133 MPa) was computed to have relatively lower von Mises stress value, at sealing pressure loads of 0.08 to 0.11 MPa, than 3A (fails at 0.114 MPa).

The von Mises stress is a failure criterion used to predict the yielding of the isotropic material under the pressure load, in which said yielding starts when the critical value for the elastic energy distortion is reached¹⁹. A higher von Mises value would mean that the material is near the yield point. In the case of the valve unit, structure A values were seen to be bigger than structure B. A smaller von Mises stress is better for a more durable device, which led us to choose structure 3B in the fabrication of the high-throughput microfluidic chip.

The von Mises stress failure criterion is related to strain energy density which tells the failure of the material once the distortional strain energy exceeds a critical value, which in turn depends on the design parameters²⁰. The strain energy density function (W) or the stored energy density refers to the energy stored in the material per unit volume of the original geometry as a function of strain at that material point. This is defined by the following equation²¹:

$$W = f(I_1, I_2, I_3) \quad (1)$$

$$= f((\lambda_1^2 + \lambda_2^2 + \lambda_3^2), (\lambda_1^2 \lambda_2^2 + \lambda_2^2 \lambda_3^2 + \lambda_3^2 \lambda_1^2), (\lambda_1^2 \lambda_2^2 \lambda_3^2))$$

where I_1, I_2, I_3 are strain invariants of Green deformation tensor. Individual strain invariants are a function of the principal stretch ratios ($\lambda_i, i = 1, 2, 3$).

Lower values of strain energy density in structure 3B is possibly due to its smaller valve cavity volume, as reflected by its smaller R_u , and the volume of pressurized gas that it holds. The low values of strain energy density would mean low risk of material failure. The shear stress and stored energy density for different loads between structures A and B are shown in Fig. S5 of the supplementary material.

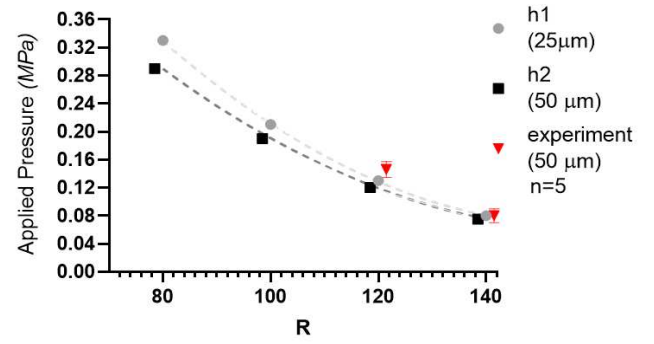


Figure 2. Relationship of the valve radius R and height h to the sealing pressure.

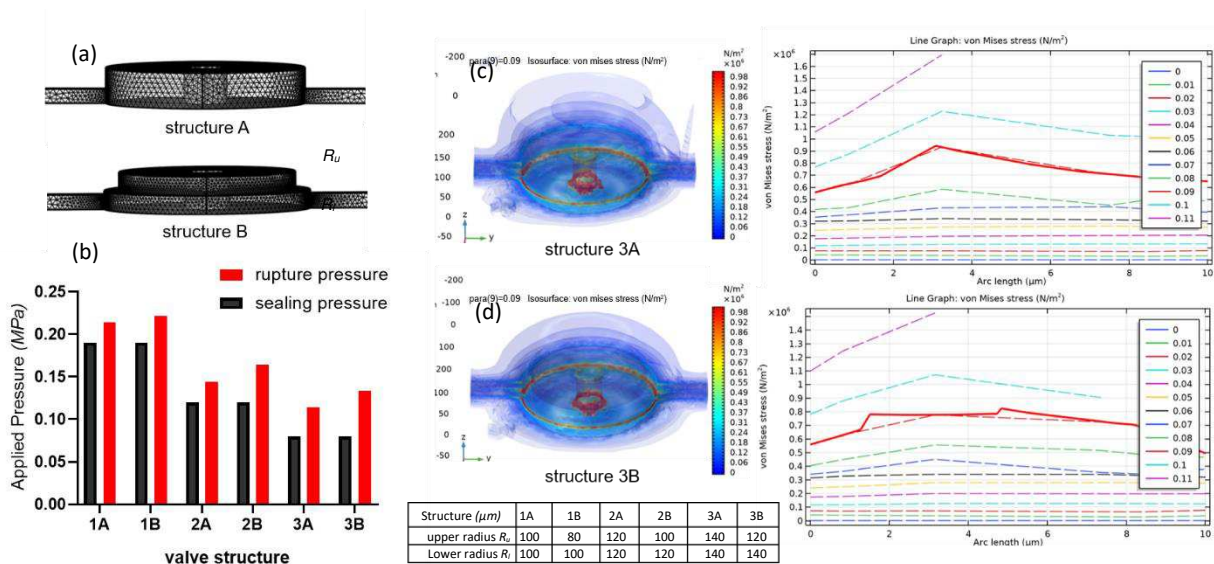


Figure 3. Effect of the valve structure on sealing pressure and rupture pressure/computation failure (a) mesh geometries of valve structures (b) comparison of the sealing and rupture pressures by valve structures (c) 3D modeling and line graph of the von Mises stress in structure 3A and (d) structure 3B.

Hydrodynamic Trapping. As previously mentioned, the maximum R of the valve that was included in the modelling was kept at $140 \mu\text{m}$ so as to keep the distance between adjacent mechanical traps around $300 \mu\text{m}$. This limitation was imposed to avoid further decrease in the single cell trap occupancy rate.

The previous version of the fabricated device, reported elsewhere²², had 1080 traps and corresponding chambers. In order to have a higher throughput and better representation of the sample population, the microfluidic chip was expanded up to 5000 traps/chambers. To determine how many single cells can be mechanically trapped, we allowed $100 \mu\text{L}$ of Jurkat cells at a concentration of 10^6 ml^{-1} to flow in the flow channel at different flow rates using a syringe pump.

Shown in figure 4 is the result of the cell trapping test that was conducted. At $30 \mu\text{L min}^{-1}$ flow rate, the chip attained 61% single cell trap occupancy, about 12% had double-cell occupancy and 6% with more than 2 cells. At 20 and $40 \mu\text{L min}^{-1}$ flow rates, about 54% and 53% of the traps were occupied by one cell. The double cell occupancy is at 7% and 6%, respectively, while $\approx 2\%$ have more than 2 cells. The single cell trap occupancy further decreased to about 47% and 45% at flow rates of 10 and $50 \mu\text{L min}^{-1}$, respectively. 10% and 6% contain two cells while 2% and 1% contain more than two cells for respective flow rates of 10 and $50 \mu\text{L min}^{-1}$. On the other hand, increasing the concentration and volume of the cell suspension introduced into the chip can increase the trap rate and reach up to 80% trap occupancy. The flow rate of $30 \mu\text{L min}^{-1}$ was later on used in the assay experiment and traps with more than 1 cell were excluded from the data evaluation process.

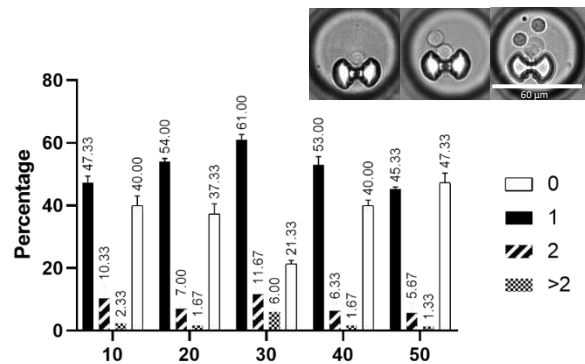


Figure 4. Percentage of trap occupancy at different flow rates. The percentage of traps with single capture is shown as a black solid bar, double capture as diagonal-patterned bar, and traps with more than 2 cells is shown as chequered bar. Only traps with single cell were analyzed. Inset, representative images of the captured cells.

Structure Reinforcement. Because of its viscoelasticity, thermosetting and inert properties, PDMS is a popular choice in the fabrication of microfluidic devices. This flexible silicone-based organic material is a viable hyperelastic material for COMSOL Multiphysics simulation, which helps explain the effects of the design parameters in valve actuation and compartmentalization²¹. Similarly, the fabricated microfluidic device is made up mostly of PDMS with a density of $0.95^{29} \text{ p/g cm}^{-3}$ and a Young's modulus, E , that is thickness dependent because of the reordering of the polymer chains to form cross-linked networks²³. The degree of cross-linking is related to the elastomer base-curing agent ratio. In this work, the flow and control layers are composed of a 10:1 and 5:1 ratio, respectively.

The elastic modulus, E , in MPa can be expressed as a function of the PDMS base/curing agent weight ratio, N , as¹⁶:

$$E = 20 \text{ MPa}/N, \quad (2)$$

Wang et. al measured E for a 5:1 ratio to be about 3.58 MPa while the 10:1 ratio is about 2.63 MPa¹³. Increasing the amount of the curing agent, such as the case of 5:1 ratio, results to a stiffer PDMS. Desai et. al modeled membrane stiffness, which can be applied to rectangular or circular membrane valves, and is given by^{23,24}:

$$k = K_{bilayer} K_{post} \frac{K_{MS}}{K_{AR}} \left(K_{shape}^1 \frac{E_{dm} t_m^3}{D^4} + K_{shape}^2 \frac{s t_m}{D^2} \right), \quad (3)$$

where k is static membrane stiffness per membrane unit area, E_{dm} is biaxial stiffness, t_m the total thickness of the membrane, D the membrane diameter or length, $K_{bilayer}$ is bilayer setup factor, K_{post} cylindrical support post factor, K_{MS} membrane stress effect (when membrane deflection exceeds half its thickness), K_{AR} aspect ratio factor, K_{shape} shape of channels factor (rectangular or circular), and s is residual stresses²³.

Generally, PDMS is a soft elastomer material that is susceptible to buckling under pneumatic or hydrostatic loading. At high pressure inputs, the valve chamber walls undergo large deformations, especially on the thin membrane walls (i.e. bottom of the valve cavity) as shown in figure 5. Although above the valve channel is a thicker and stiffer control layer, change in geometry (displacement field) is observable as a result of the valve actuation.

In order to reduce the volume expansion on top of the valve cavity, consequentially reduce deformation and strain on the portions of the structure that is not critical for bending, a custom fabrication of adding a thin glass sheet as reinforcement (Matsunami coverglass; 0.13 mm – 0.17 mm thickness) about 100 μm on top of the control layer valves was done and is shown in figure 6a. This combination of materials results to an even stiffer top component. This can result to a smaller deformation or volume change.

The reduction of the expansion volume of non-critical actuator sections can increase the speed at which the softer membrane at the bottom bends during actuation. This in turn can reduce the sealing pressure needed to close thousands of chambers in array²⁵. At the same time, the reduced deformation and sealing pressure can result to lower material strain and improved durability.

Actuating the microvalves to seal the cell-isolating chamber at lower pressure is seen advantageous since many cells respond to pressure and mechanical strain as well as to shear stress²⁶. Several experimental observations have shown stress-dependent histological reactions of cell death, reactive oxygen species (ROS) level increases, as well as leaky vasculature²⁷. Therefore, reduction of external pressure received by cells during experiment is important in managing stress and viability of the samples.

With the new design structure and customization condition, an actuation test was done to the array of microvalves to determine the working pressure needed to seal all the microchambers. Without the glass reinforcement, the lowest pneumatic sealing pressure achieved was 0.07 MPa ($\bar{x} = 0.08$, std. dev.=0.008) as shown in figure 6b. With the addition of the glass top,

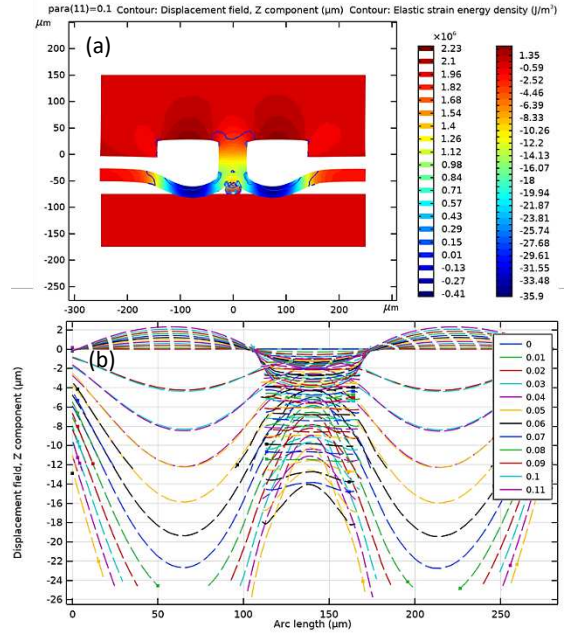


Figure 5. Displacement fields (Z) of the elastomer valve cavity under various pressure loads. (a) displacement field and elastic strain energy of 2D cut plane (b) line graph of the displacement field along the arc length.

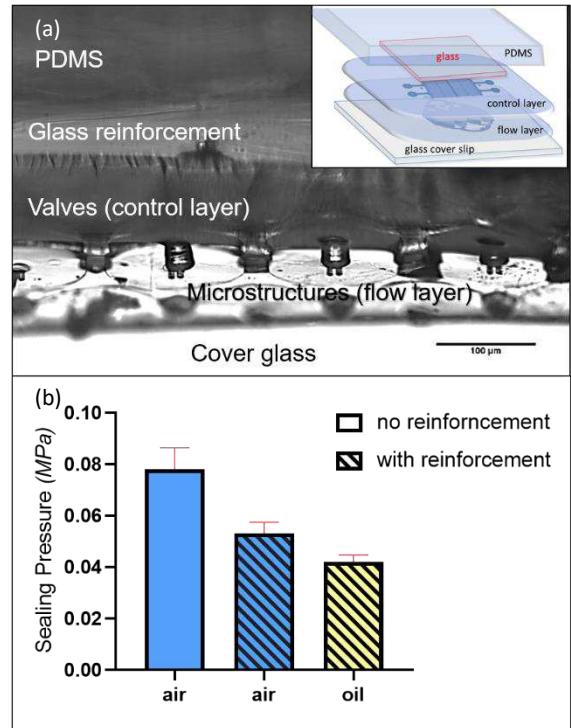


Figure 6. Reinforcement of the control layer via addition of thin glass $\approx 100 \mu\text{m}$ above the PDMS microvalves (a) cross-section image of the microfluidic device, inset: by-layer composition illustration (b) comparison of the sealing pressures at varying conditions ($n=5$).

the sealing pressure was reduced to 0.05 MPa ($\bar{x} = 0.053$, std. dev. = 0.004). We also explored the effect of the actuating media by substituting air with mineral oil (Sigma Aldrich M5904) and found that the sealing pressure was further reduced to 0.04 MPa ($\bar{x} = 0.042$, std. dev. = 0.003).

This reduction in the working pressure when oil was used as actuation medium can be due to the suppression of permeability of the thin PDMS membrane in the valve. PDMS is permeable to gases and this can cause a problem to microfluidic devices operated at high operating pressures and longer periods of time²⁸. In our experience, pneumatic valve actuations during assay experiments for many hours can result to gas bubble formation inside the fluidic channels which ruins the assay protocol (i.e. media exchange) or the entire experiment itself.

For this material, the relationship between the volumetric flow rate q , permeability coefficient P , membrane thickness t , valve radius R , and pressure difference Δp is given by²⁹:

$$P = \frac{qt}{\pi R^2 \Delta p}, \quad (4)$$

The equation above (equation 4) tells that the volumetric flow q through the PDMS membrane is inversely proportional to the thickness, which is significant for thin layers. The thickness of the membrane, which dictates its flexibility and degree of deflection, is also crucial for the valve functionality. With oil filling the valve cavities, a barrier between the pressurized gas and permeable membrane is created. In effect, this suppresses the gas permeability and reduce the sealing pressure.

Single Cell Assay. The optimization conditions and fabrication customizations explored in this work was used in the fabrication of a high throughput valve-based microfluidic device that was utilized in the single cell enzymatic activity assay experiment. The purpose of this experiment is to quantify the expression of granzyme B protein from each cell and create a profile to show the variability of said expressions.

After cell preparation, samples were introduced to the microfluidic device following experiment protocol (Fig. S4). About 3922 Jurkat cells, individually trapped and isolated in the microchambers, were assayed and its profile is shown in figure 7. With each data point representing individual cell, the graph shows the variability of protease expression at single cell level with a mean fluorescence intensity value of 27, a maximum value of 62, and a standard deviation of 14.6. The difference between the individual value was found significant using the One Sample Wilcoxon Test with a P value of <0.0001 (alpha = 0.05).

The same assay was also performed to PBMC cells from a healthy person (Fig. 8). The granzyme B activity at single cell level is found to be similarly varied with a mean value of 8, maximum of 39, and standard deviation of 7.2. A significant difference was also found using one sample Wilcoxon test with a P value of <0.0001 (alpha = 0.05), demonstrating heterogeneity in the protein expression within the sample population. Only 2730 single cells were trapped for this test as PBMC cells have smaller diameter than Jurkat, allowing for some cells to escape through the trap gap. Figure 8a shows the GrB activity according to immune cell composition of the sample, identified via antibody immunostaining for CD3 (CD4 and CD8 expressing T cells), CD56 NK cells, and double positive (NKT cells). The percentage composition of the captured immune cells is shown in figure 8b.

The GrB profile for both the Jurkat and PBMC samples shows variability of protease expression in single cell level, which is important in monitoring heterogeneity and identification of cell subsets with overexpression. From the resulting profile, specific cells that are showing unique expression patterns can be identified. Other surface markers (i.e. anti-PD1, Ig-G4) can be introduced in the chip to determine the cell state or patient response to a particular treatment (i.e. immunotherapy). The information that can be gathered from the behavior of each cell, in general, or from individual immune cell, in particular, can lead to discoveries of several biological functions that are not observed in bulk analysis. This single cell analysis can provide information on genotype, phenotype, protein secretion, proliferation, maturation, activation, signaling pathways of each activated cell, and the intercellular communication among different immune cells^{2,24}.

Conclusion

In order to improve the throughput of the valve-based microfluidic device, optimization of the valve design and fabrication technique was sought. Design modeling through COMSOL Multiphysics was done to determine the valve dimension and geometry that could result to lower sealing pressure. Optimization in the fabrication technique was also pursued through the addition of a glass slip a few microns above the valve cavities in order to increase the stiffness and reduce the strain of the top portion. The effect of air and oil as actuation media to the sealing of the microchambers was also compared.

Applying these optimization conditions resulted to the fabrication of a microfluidic device composed of 5000 circular microvalves that can be actuated at a pressure as low as 0.04 MPa to seal all chambers. The reduction in the working pressure

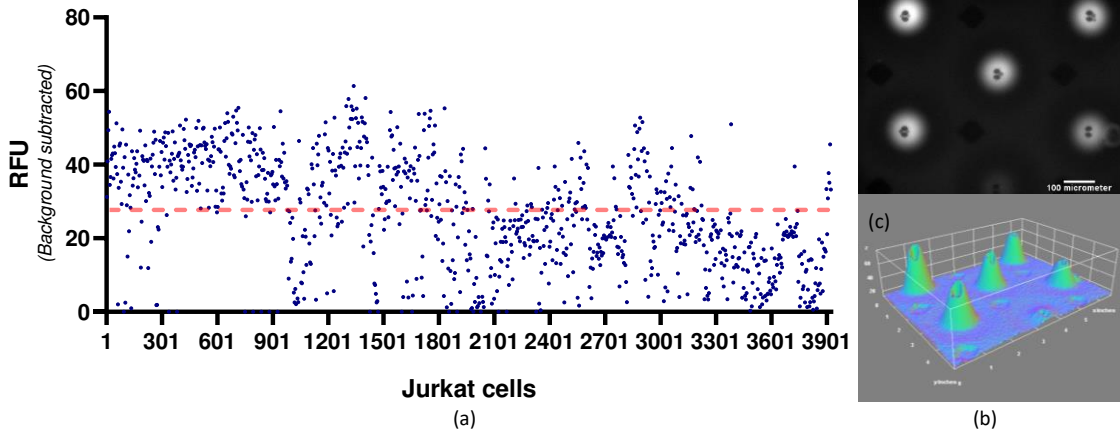


Figure 7. Single cell fluorometric granzyme B activity assay for Jurkat cells (a) graph showing cell expression profile (dashed line indicates the mean value) (b) monochrome image of the microchambers showing the fluorescence (white) from AFC fluorophore (c) 3D surface plot of the same microchambers using ImageJ software.

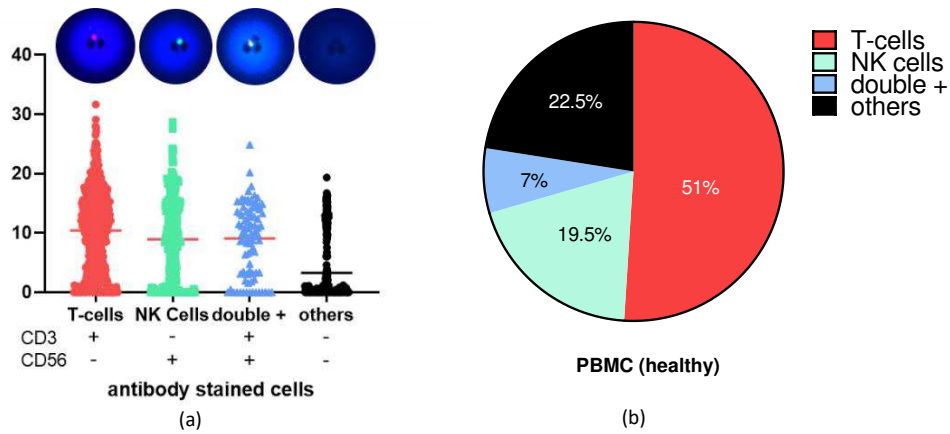


Figure 8. Single cell fluorometric granzyme B activity assay for PBMC cells from healthy person (a) antibody staining shows the immune cell composition and corresponding activity (red line indicates the mean value) (b) percent composition of immune cells in the profiled sample.

is seen significant as it gives more room to increase the number of valves that can be added to the chip and thus further increasing the throughput. Higher throughput devices give a better representation of the sample population and is suited for single cell analysis experiments that look into heterogeneities and identify unique cell subsets or super mutants from thousands of cells. This provides insightful information to researchers and clinicians on the cell of interest, which can lead to drug discovery and improvement in treatment personalization.

Methods

Multiphysics modeling. The model formulated in this work was developed to describe the pneumatic operation of the microchamber block. The geometry and specifications shown in Figure 9a and Table 1 were used in modeling the microvalve, constructed using the COMSOL Multiphysics (ver5.5) simulation tool. Since the expression level of granzyme B per cell is low, the resulting chamber volume was kept to less than 100 picolitre in order to isolate a higher concentration of the biochemical agent^{14,15}. Thus, the valve's inner radius was set to 30 μm . Meanwhile, the valve's outer radius (R), height (h), and overall structure was varied to gain insight into the dependence of the actuation/sealing pressure on the geometry of the valve.

The membrane deflection in the microchamber block of the microfluidic device was simulated using the laminar flow and solid mechanics modules. The laminar flow for fluid flow physics was used for valve channel in which stationary simulation for weakly compressible flow was carried out to obtain the fluid velocity and pressure profile. Air was used as the fluid for the simulation.

The solid mechanics for structural mechanics physics was used for the elastomer membrane deflection to determine the relation of the valve diameter and height to the sealing pressure. PDMS was modeled as a linear elastic material with elastic modulus of 2.63 MPa (for a 10:1 pre-polymer/curing agent ratio¹⁶), a Poisson's ratio of 0.49 and a density of 950 kg/m^3 . The Neo-Hookean model was used for the hyperelastic, near-incompressible, material with Lamé parameter, μ , of $6.67 \times 10^5 \text{ N}/\text{m}^2$

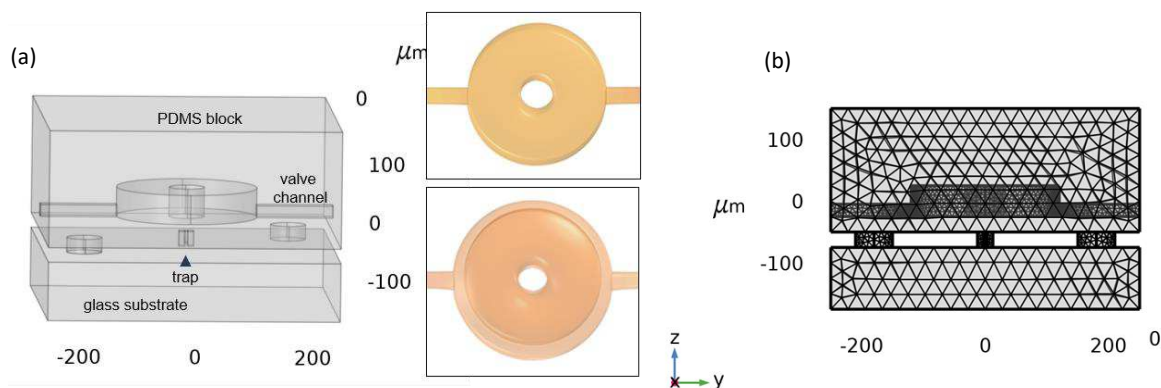


Figure 9. Microfluidic chamber block comprising of the control microvalve and mechanical trap (a) COMSOL rendered valve geometries (b) physics-controlled finer mesh model.

and bulk modulus, κ , of 3.33×10^7 Pa. This constitutive model describes the behavior of a rubber-like material undergoing large deformation which is obtained by a statistical-mechanical deformation treatment of freely jointed molecular chains. A glass block was placed at the bottom part of the chamber model, representing a glass substrate, and set as a fixed constraint. All other material properties for the simulation was taken from the COMSOL material library. The physics-controlled finer mesh was used and is shown in Figure 9b.

Device fabrication. Identified optimal parameters from the simulation analysis were applied in the device fabrication. To fabricate and assemble the microfluidic device, two molds on a 4" silicon wafers were created, following its corresponding CAD design, using optical photolithography. For the flow layer mold, SU8 3010 and 3025 photoresists (MicroChem, Massachusetts, USA) were spin coated at different steps to fabricate structures of varying heights (15 μm and 25 μm). Meanwhile, SU8 3025 was used for the control layer mold following the same steps to create microstructures of 25 μm and 50 μm . The resists were then exposed to UV light source (20,000 mJ cm^{-2} at 405 nm) using a maskless exposure apparatus (Nano System Solutions DL-1000). The molds were then developed and subsequently silanized with 1H,1H,2H,2H-perfluorodecyltrichlorosilane (Wako Pure Chemical Industries, Ltd.) for ease of release of PDMS from the mold. Figures 10a and 10b shows the CAD design of the flow and control layers.

The microfluidic chip was then created through pattern transfer using PDMS. A 10:1 ratio of PDMS oligomer and curing agent (Sylgard 184 silicone elastomer kit, Dow Corning, USA) was spin coated on the flow layer mold to produce about 50 μm thick PDMS layer. Meanwhile, a 5:1 ratio was coated on the control layer mold to create a thicker layer. After partially curing at 80 $^{\circ}\text{C}$ for 15 minutes, the two PDMS layers were peeled, cut to size, and aligned. Since the elastomer flow layer is very thin to be handled without damage, the thick control layer is first removed from its mold and aligned on top of the flow layer. The remaining 5:1 PDMS mixture was poured around the aligned layers and then cured for 2 hours at 80 $^{\circ}\text{C}$. Here, excess functional groups in the two layers interact to form a covalent bond across the interface, resulting to an irreversible bonding of the two layers¹⁷. The PDMS chip was finally bonded to a cleaned microscopy coverslip after exposure to oxygen plasma for 50 s in a Plasma Dry Cleaner (Yamato PDC210) at maximum power (75 W). The resulting microfluidic device is shown in figure 2c. The thin flow layer at the bottom has microstructures that serves as hydrodynamic traps for single cells while the thick control layer on top has circular pneumatic microvalves that can be actuated to create a sealed microchamber (Fig. 10d and 10e). An outline of the fabrication steps for mold fabrication and PDMS device assembly is shown in Fig. S1 and S2 of the supplementary material.

Valve actuation and chamber sealing. To form a sealed microchamber with a trapped cell inside, we made use of a circular microvalve design and actuate it with positive pressure using an air pump (ULVAC DA-60S). This shape was chosen as rectangular valves can cause leak at the corners of the channel valve intersection (Fig. S3). Microfluidic valves are usually formed when the control channel crosses the fluid channel. In a square or rectangular profile, the gaps created at incompletely closed corners during actuation are large enough to allow fluids to pass¹⁸. A comparison of an actuated circular and rectangular valve is shown in the supplementary material.

Table 1. Specifications of the microvalve used for simulation

valve unit	inner radius, r (μm)	outer radius, R (μm)	height (μm)
A	30	80	25
B		100	
C		120	
D		140	
E	30	80	50
F		100	
G		120	
H		140	

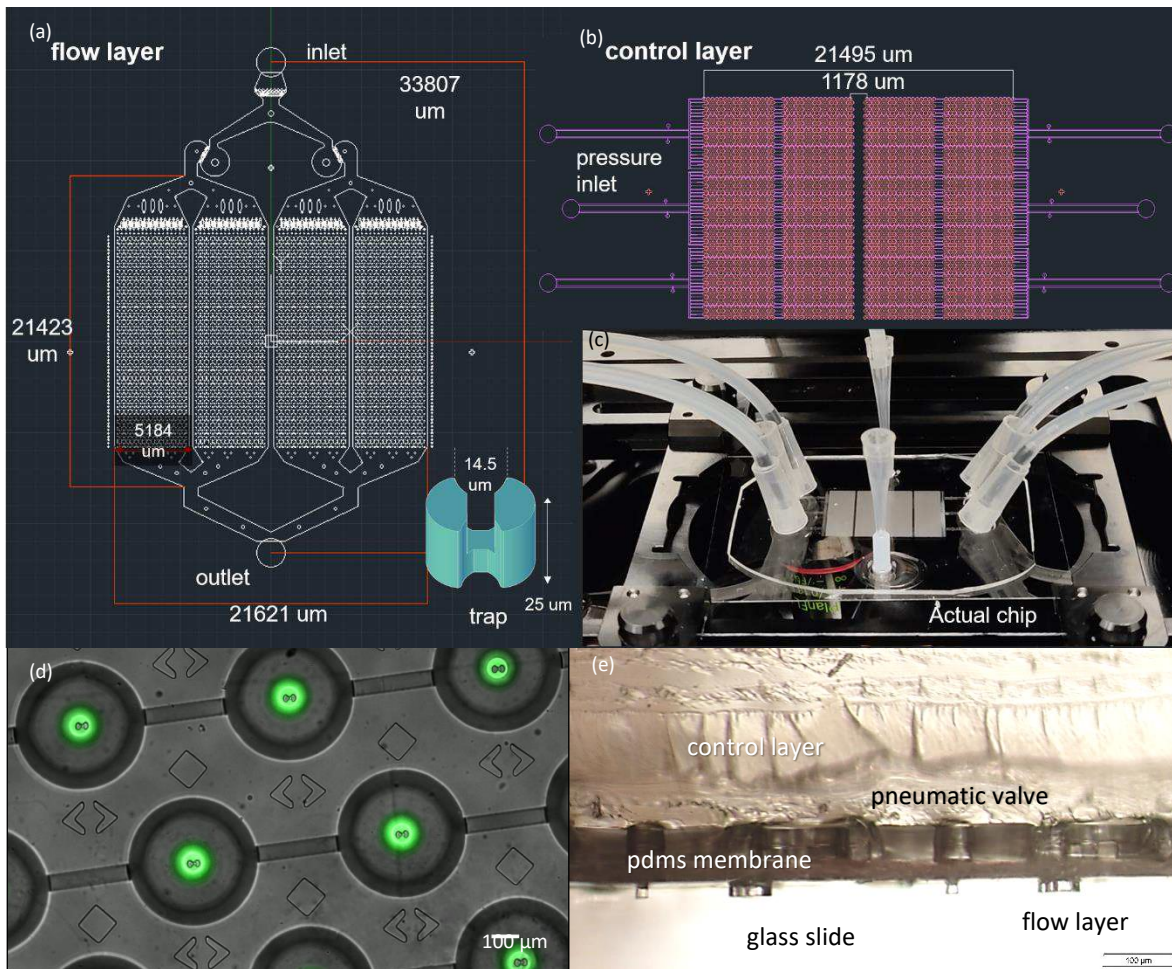


Figure 10. Microfluidic chip design for high throughput single cell assay (a) CAD design of the flow layer (inset) hydrodynamic trap design (b) CAD design of the control layer (c) photo of the assembled microfluidic device (d) microscope image of an array of actuated valves confining a fluorescent solution (e) microscope image of the chip's cross-section.

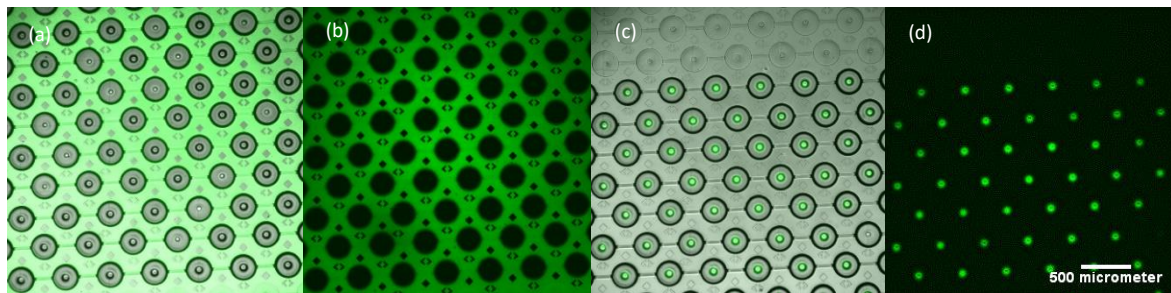


Figure 11. FITC dextran fluorescence solution was used to check the sealing of the microchambers. The solution was made to flow into the channels and the microvalves were actuated (a) multicolor image of the channel and valve array (b) image under FITC (488) filter. After opening-closing the microvalves, the channel was washed by flowing PBS while the valves are actuated leaving the fluorescent solution trap inside the chamber (c) multicolor image (d) image under FITC (488) filter.

A sealed microchamber was determined by filling the flow channels with fluorescent solution FITC dextran (1 mg ml^{-1} , Sigma-Aldrich) and actuating the valves afterwards (Fig. 11). The fluorescence at the actuated valve area of the chamber is measured and compared to the intensities of the areas without valve actuation under varying applied pressure. The effect of varying conditions (i.e. structure and actuation media) to the sealing pressure was compared.

Device operation and single cell assay. The microfluidic device was used to conduct single cell assay using Jurkat T-lymphocyte cell and human peripheral blood mononuclear cell (PBMC). Granzyme B (GrB)-overexpressing Jurkat cells, provided by the collaborators from Osaka University Hospital, were generated by lentiviral transduction of expression plasmid. The cell samples were expanded from a cryopreserved master cell bank and maintained in a 10% fetal bovine serum (Gibco FBS, Thermo Fisher Scientific) medium and 1% penicillin in RPMI (Gibco RPMI 1640, Thermo Fisher Scientific). The

cultures were stored in an incubator at 37°C and 5% CO₂ prior to conducting the assay experiment. The handling and experiments on cell samples were performed in accordance with the protocols of the Research Safety Committee of Osaka University.

To reduce cell adhesion on the channel walls, the microfluidic chip was blocked with 1% BSA (bovine serum albumin, Sigma-Aldrich, USA) in PBS solution for 1 hour. Using a syringe pump, the chip was washed with PBS for 10 min at a flow rate of 50 $\mu\text{L min}^{-1}$. In the conduct of the assay experiment, a cell suspension was flushed into the chip at a flow rate of 30 $\mu\text{L min}^{-1}$ to be captured by the hydrodynamic traps. Excess cells were flushed out by rinsing the chip with 50 μL of buffer medium. Afterwards, the control channels and microvalves were actuated to seal the microchambers and isolate each trapped cell. A granzyme B recognition substrate (Ac-IEPD-AFC) in buffer from a commercial assay kit (Promocell GmbH, Heidelberg, Germany) was introduced into the microchambers by briefly opening and closing the valves. After 30 minutes incubation, the expressed GrB molecules from individual cells were quantified fluorometrically through the cleaving of the peptide substrate. A fluorescence microscope (BZ-X810, Keyence; 2/3 inch, 2.83 million-pixel monochrome CCD camera) was used to observe and capture the images of the microchambers. PH and DAPI (360/460nm) filters were used during image acquisition. The acquired images were then analyzed and quantified for its fluorescence intensity using ImageJ image analysis software.

Immunostaining was also performed to PBMC cells for cell surface markers CD3 (CD4 and CD8 expressing T cells, Alexa Fluor 532) and CD56 Natural Killer (NK) cells (Alexa Fluor 488). This is to identify the immune cell composition of the sample. An outline of the single cell assay experiment can be found in the supplementary material (Fig. S4).

References

1. Kulasingham A., Wu H., Punyadeera C., & Warkiani M.E. The Use of Microfluidic Technology for Cancer Applications and Liquid Biopsy. *Micromachines* **9**, 397 (2018).
2. Sinha N., Subedi N., & Tel J. Integrating Immunology and Microfluidics for Single Immune Cell Analysis. *Front. Immunol.* **9**, 2373 (2018).
3. An X., & Varadarajan N. Single-cell technologies for profiling T cells to enable monitoring of immunotherapies. *Curr. Opin. Chem. Eng* **19**, 142 (2018).
4. Sun G., & Lu H. Recent Advances in Microfluidic Techniques for Systems Biology. *Anal. Chem.* **91** (1), 315 (2019).
5. Murphy T. W., Zhang Q., Naler L. B., Ma S., & Lu C. Recent advances in the use of microfluidic technologies for single cell analysis. *Analyst* **143**, 60 (2018).
6. Au A.K., Lai H., Utela B. R., & Folch A. Microvalves and Micropumps for BioMEMS. *Micromachines* **2**(2), 179 (2011).
7. Lau A.T.H., Yip H. M., Ng K.C.C., Cui X., & Lam R.H.W. Dynamics of Microvalve Operations in Integrated Microfluidics. *Micromachines* **5**(1), 50 (2014).
8. Blazek M., Betz C., Hall M.N., Reth M., Zengerle R., & Meier M. Proximity ligation assay for high-content profiling of cell signaling pathways on a microfluidic chip. *Mol Cell Proteomics* **12**(12), 3898 (2013).
9. Armbrrecht L., Müller R.S., Nikoloff J., & Dittrich P.S. Single-cell protein profiling in microchambers with barcoded beads. *Microsyst Nanoeng* **5**, 55 (2019).
10. Kellogg R., Gómez-Sjöberg R., Leyrat A., & Tay S. High-throughput microfluidic single-cell analysis pipeline for studies of signaling dynamics. *Nat Protoc* **9**(7), 1713 (2014).
11. Tong A. *et al.* Automated Addressable Microfluidic Device for Minimally Disruptive Manipulation of Cells and Fluids within Living Cultures. *ACS Biomaterials Science & Engineering* **6** (3), 1809 (2020).
12. Payne E., Holland-Moritz D., Sun S., & Kennedy R.T.. High-throughput screening by droplet microfluidics: perspective into key challenges and future prospects. *Lab Chip* **20**, 2247 (2020).
13. Sundberg S.A. High-throughput and ultra-high-throughput screening: solution- and cell-based approaches. *Current Opinion in Biotechnology* **11** (1), 47 (2000).
14. Mahrus S. & Craik C.S. Selective chemical functional probes of granzymes A and B reveal granzyme B is a major effector of natural killer cell-mediated lysis of target cells. *Chemistry & Biology* **12**(5), 567 (2005).
15. Lin L. *et al.* Granzyme B secretion by human memory CD4 T cells is less strictly regulated compared to memory CD8 T cells. *BMC immunology* **15**(36) (2014).
16. Wang Z., Volinsky A.A., & Gallant N.D. Crosslinking effect on polydimethylsiloxane elastic modulus measured by custom-built compression instrument. *J. Appl. Polym. Sci.* **131**(22) (2014).
17. Lai A., Altemose N., White J.A., & Streets A.M. On-ratio PDMS bonding for multilayer microfluidic device fabrication. *J Micromech Microeng* **29**(10) (2019).
18. van Dam R. M. *Solvent-Resistant Elastomeric Microfluidic Devices and Applications*. Ph.D. thesis, California Institute of Technology, Pasadena, 2006.
19. Gidde R.R. & Pawar P.M. On effect of viscoelastic characteristics of polymers on performance of micropump. *Advances in Mechanical Engineering* **9**(2) (2017).

20. Jung J., Hwang I., & Lee D. Contact Pressure and Strain Energy Density of Hyperelastic U-shaped Monolithic Seals under Axial and Radial Compressions in an Insulating Joint: A Numerical Study. *Appl. Sci.* **7**(8), 792 (2017)
21. Galley A. *Pneumatic Hyperelastic Robotic End-Effector for Grasping Soft Curved Organic Object*. Master's thesis, The University of Western Ontario Electronic Thesis and Dissertation Repository, 2019.
22. Briones J.C. *et al.* A Microfluidic Platform for Single Cell Fluorometric Granzyme B Profiling. *Theranostics* **10** (1), 123 (2020).
23. Desai A.V., Tice J. D., Apblett C. A., & Kenis P. J. Design considerations for electrostatic microvalves with applications in poly(dimethylsiloxane)-based microfluidics. *Lab Chip* **12**(6), 1078 (2012)
24. Chao M., Harris J., Morales R. T., Chen W., & Jiang X. (eds). *Microfluidics for Immuno-oncology in Nanofluidics and Microfluidics* 1st edn. (Wiley-VCH Verlag GmbH & Co. KGaA, Weinheim, 2020) pp 149-176.
25. Mosadegh B. *et al.* Pneumatic Networks for Soft Robotics that Actuate Rapidly. *Adv. Funct. Mater.* **24** (15) 2163 (2014).
26. T. Satoh *et al.* A pneumatic pressure-driven multi-throughput microfluidic circulation culture system. *Lab Chip* **16**, 2339 (2016).
27. Ahn J. *et al.* Pneumatically Actuated Microfluidic Platform for Reconstituting 3D Vascular Tissue Compression. *Appl. Sci.* **10** (6), 2027 (2020).
28. Goldowsky J. & Knapp H.F. Gas penetration through pneumatically driven PDMS micro valves. *RSC Adv.* **3**, 17968 (2013)
29. Marjani A., Abkhiz V., & Fadaei F. Computational simulation of gas separation using nonporous polymeric membranes: Experimental and theoretical studies. *Polymer Engineering & Science* **55**(1), 54 (2015).

Acknowledgements

This work was supported by the Core Research for Evolutionary Science and Technology (CREST) Program with JST CREST Grant Number JPMJCR16G2, Japan.

Author contributions statement

Briones J. performed experiment, and result interpretation. Espulgar W. performed modeling, simulation, and result interpretation. Koyama S. methodology. Takamatsu H. sample preparation, data analysis, and methodology. Tamiya E, supervision. Saito M. research conceptualization. All authors assisted in data analysis and reviewed the manuscript.

Additional information

The authors declare no competing interests.

Supplementary information is available for this paper.

Figures

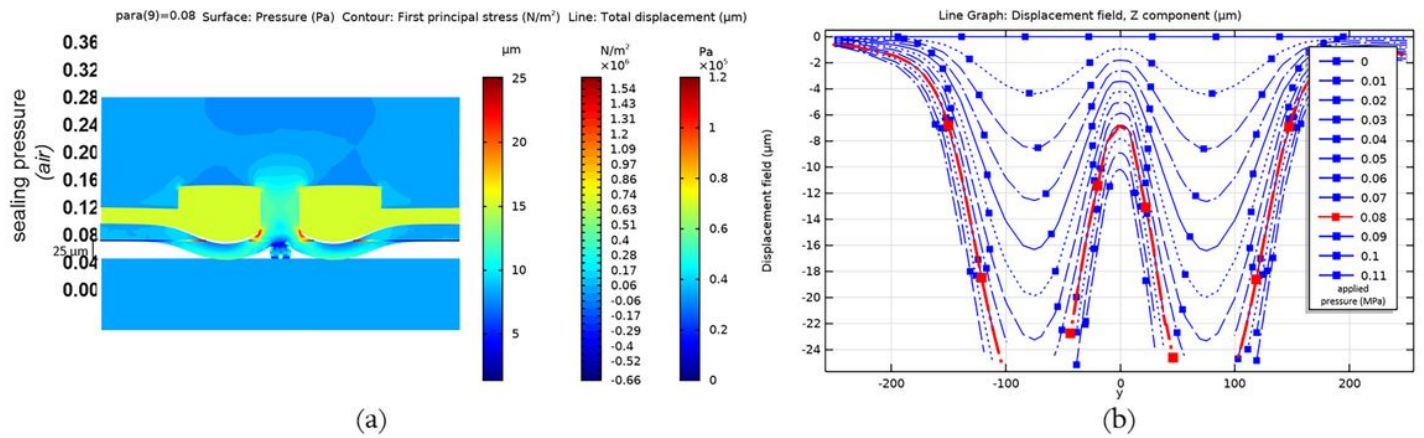


Figure 1

Multiphysics simulation of the unit valve's ($R=140 \mu$, $h=50$) actuation. (a) 2D plot of the middle cut plane indicating membrane deflection, resulting surface pressure and first principal stress (b) line graph of the displacement field at various applied pressure (MPa) across the arc length.

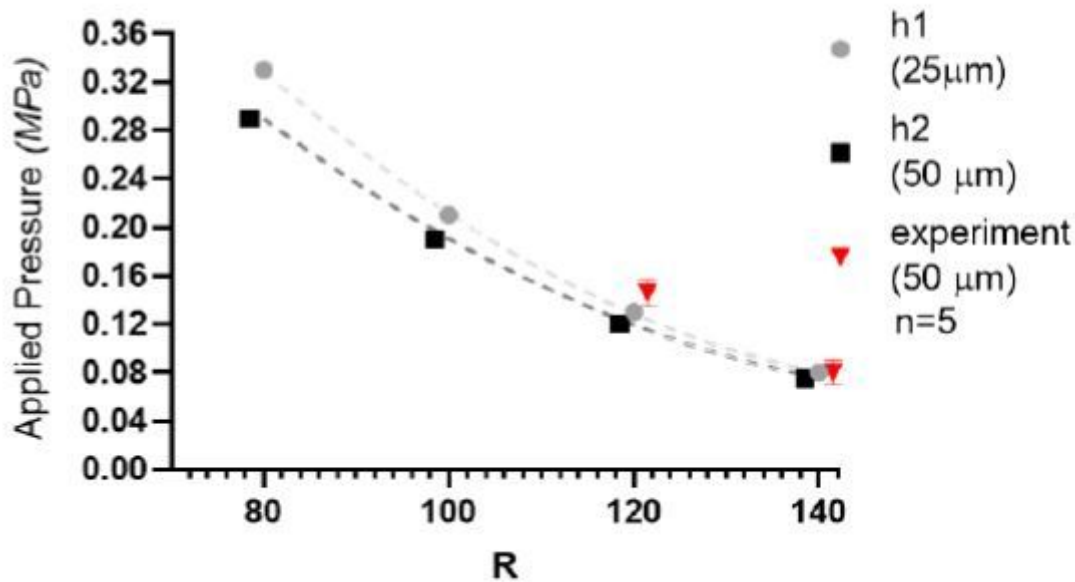


Figure 2

Relationship of the valve radius R and height h to the sealing pressure.

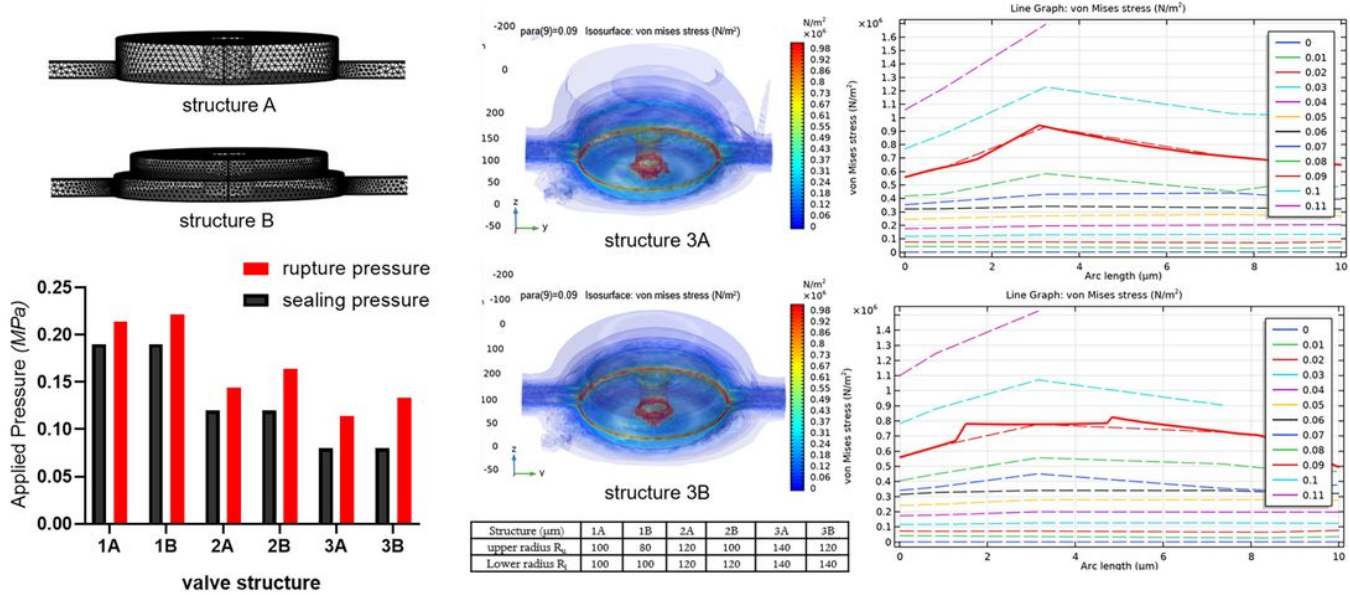


Figure 3

Effect of the valve structure on sealing pressure and rupture pressure/computation failure (a) mesh geometries of valve structures (b) comparison of the sealing and rupture pressures by valve structures (c) 3D modeling and line graph of the von Mises stress in structure 3A and (d) structure 3B.

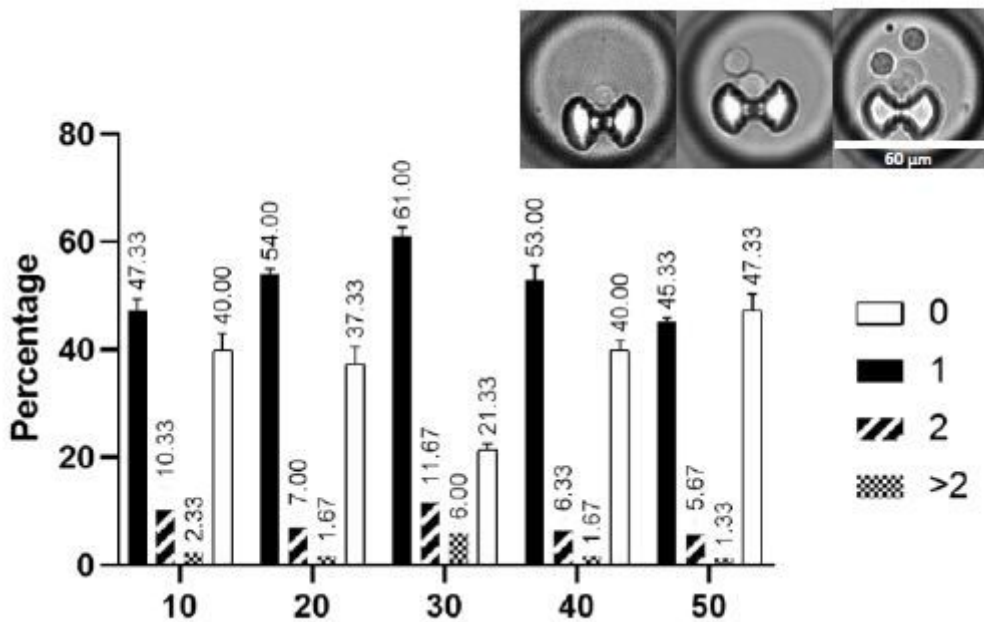


Figure 4

Percentage of trap occupancy at different flow rates. The percentage of traps with single capture is shown as a black solid bar, double capture as diagonal patterned bar, and traps with more than 2 cells is

shown as chequered bar. Only traps with single cell were analyzed. Inset, representative images of the captured cells.

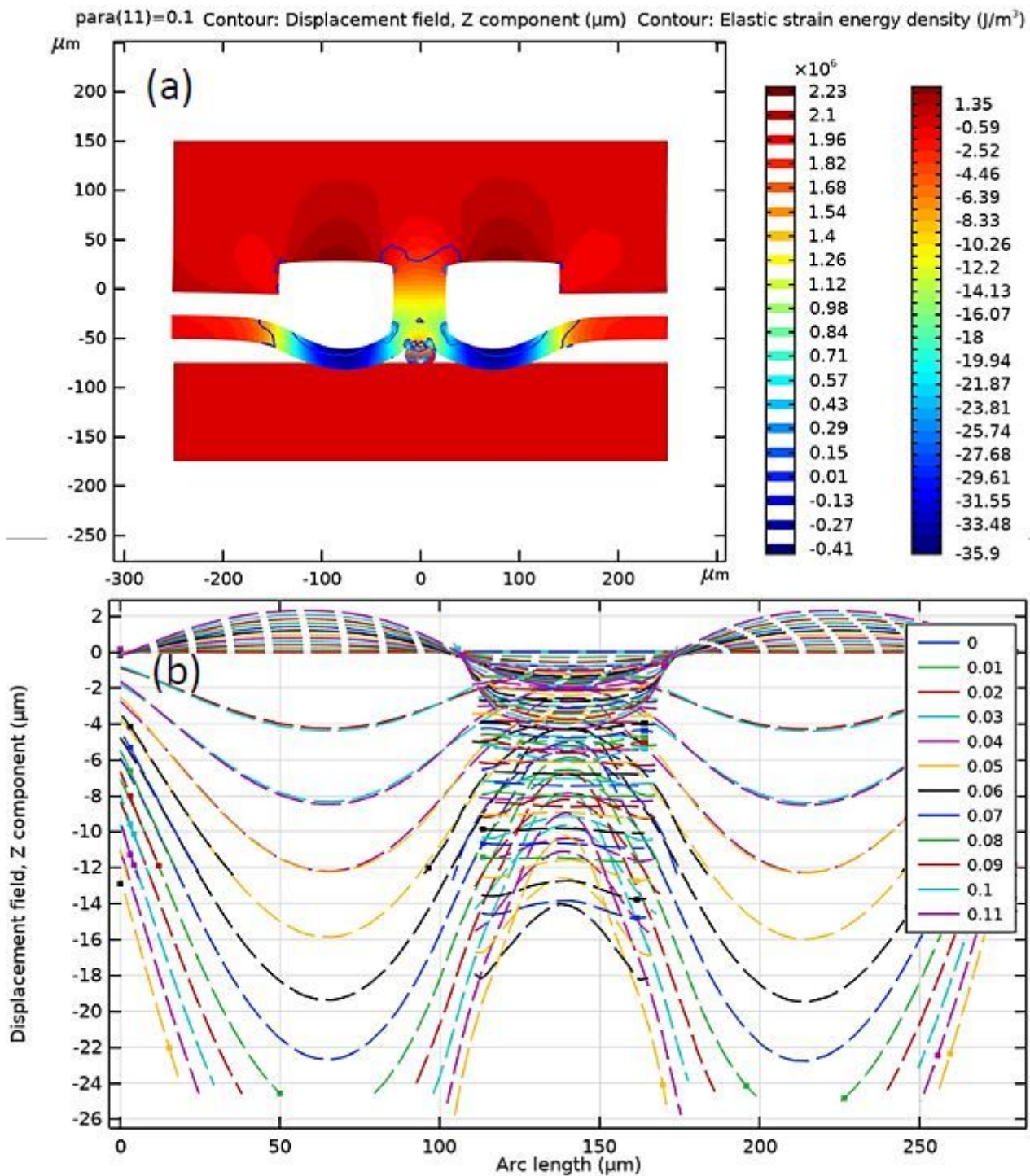


Figure 5

Displacement fields (Z) of the elastomer valve cavity under various pressure loads. (a) displacement field and elastic strain energy of 2D cut plane (b) line graph of the displacement field along the arc length.

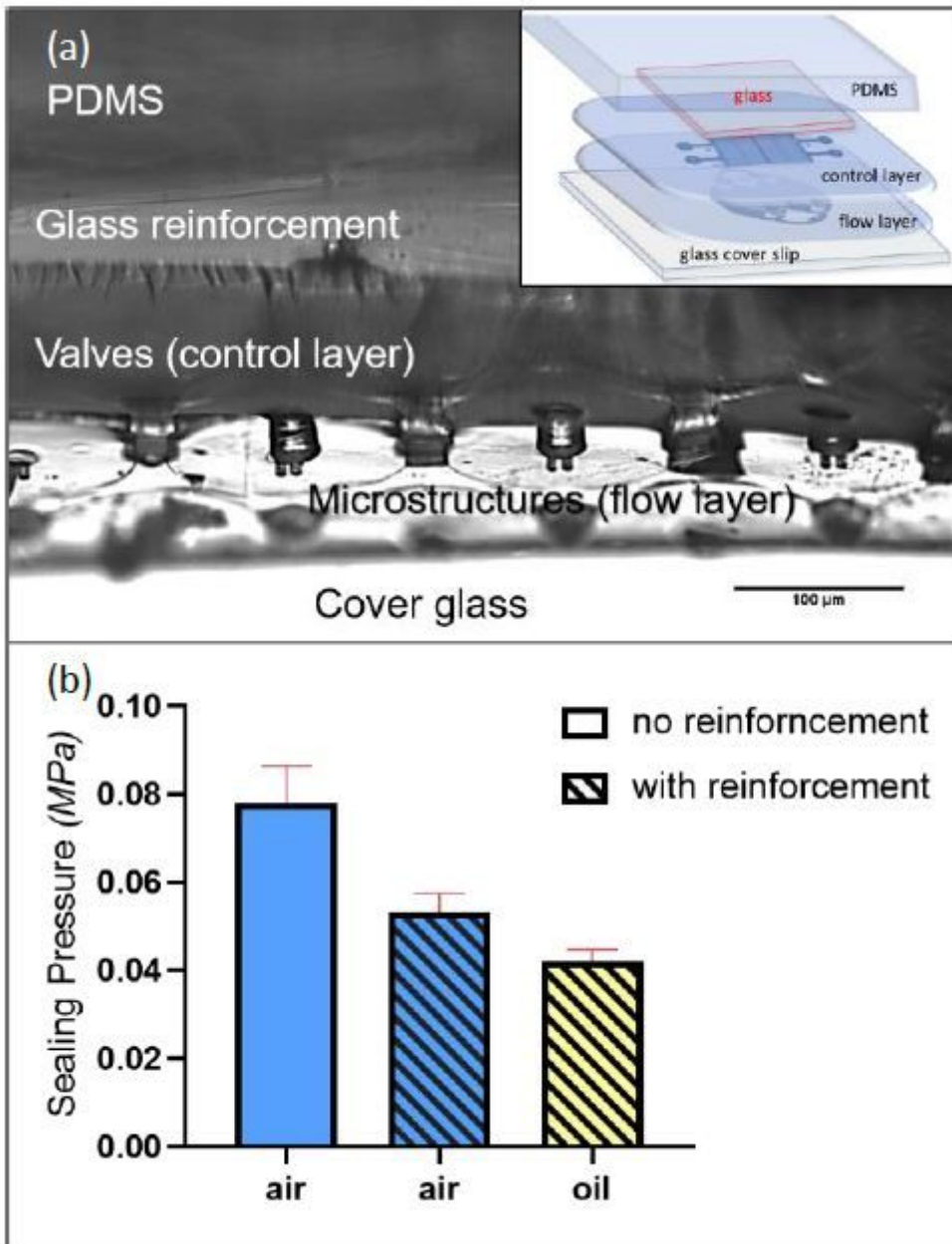


Figure 6

Reinforcement of the control layer via addition of thin glass $\approx 100 \mu\text{m}$ above the PDMS microvalves (a) cross section image of the microfluidic device, inset: by layer composition illustration (b) comparison of the sealing pressures at varying conditions (n=5).

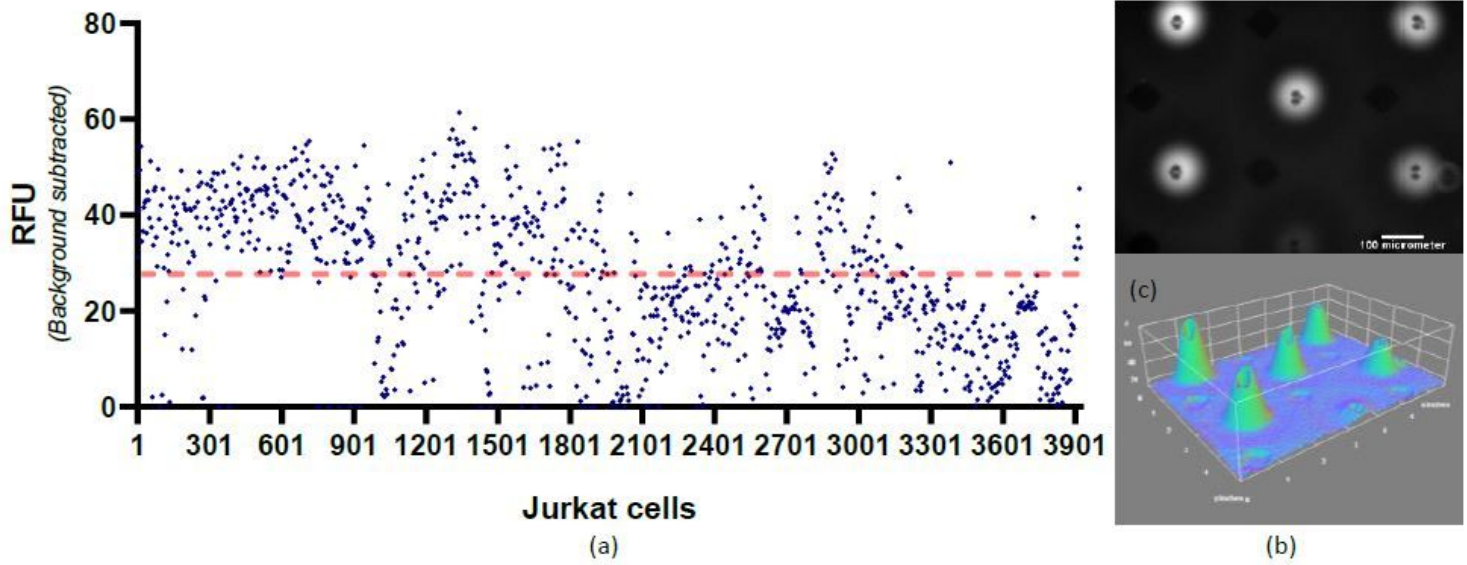


Figure 7

Single cell fluorometric granzyme B activity assay for Jurkat cells (a) graph showing cell expression profile (dashed line indicates the mean value) (b) monochrome image of the microchambers showing the fluorescence (white) from AFC fluorophore (c) 3D surface plot of the same microchambers using ImageJ software.

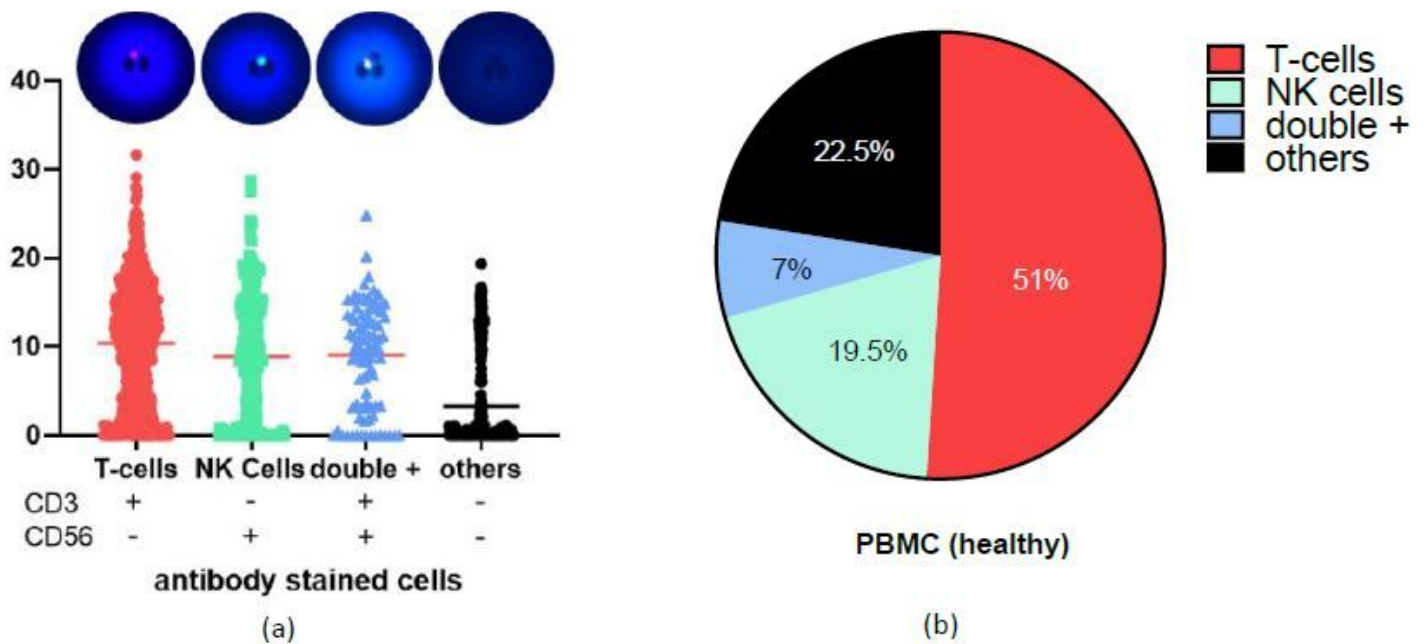


Figure 8

Single cell fluorometric granzyme B activity assay for PBMC cells from healthy person (a) antibody staining shows the immune cell composition and corresponding activity (red line indicates the mean

value) (b) percent composition of immune cells in the profiled sample.

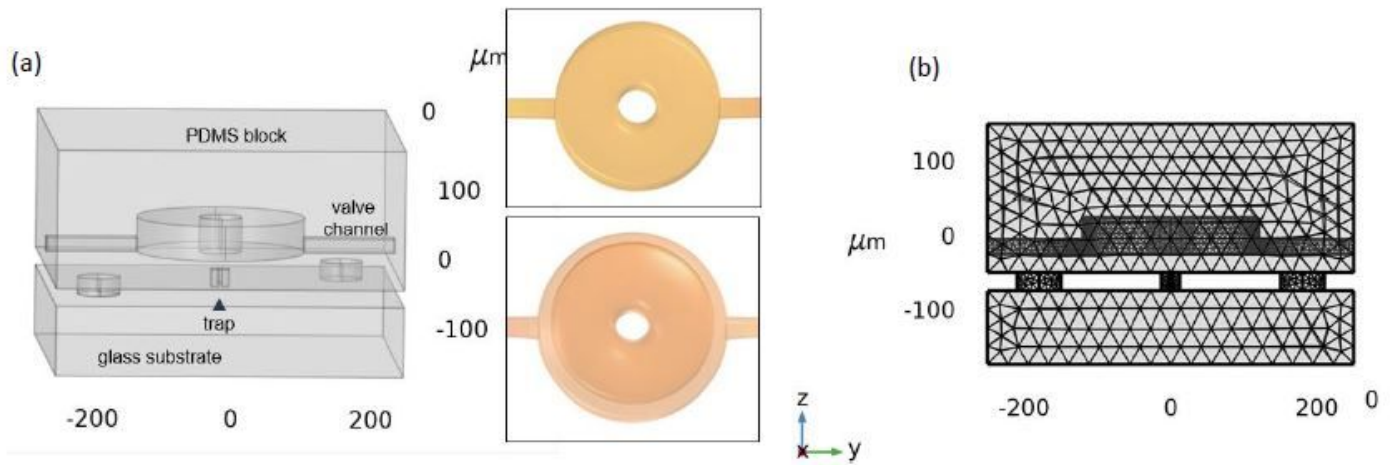


Figure 9

Microfluidic chamber block comprising of the control microvalve and mechanical trap (a) COMSOL rendered valve geometries (b) physics controlled finer mesh model.

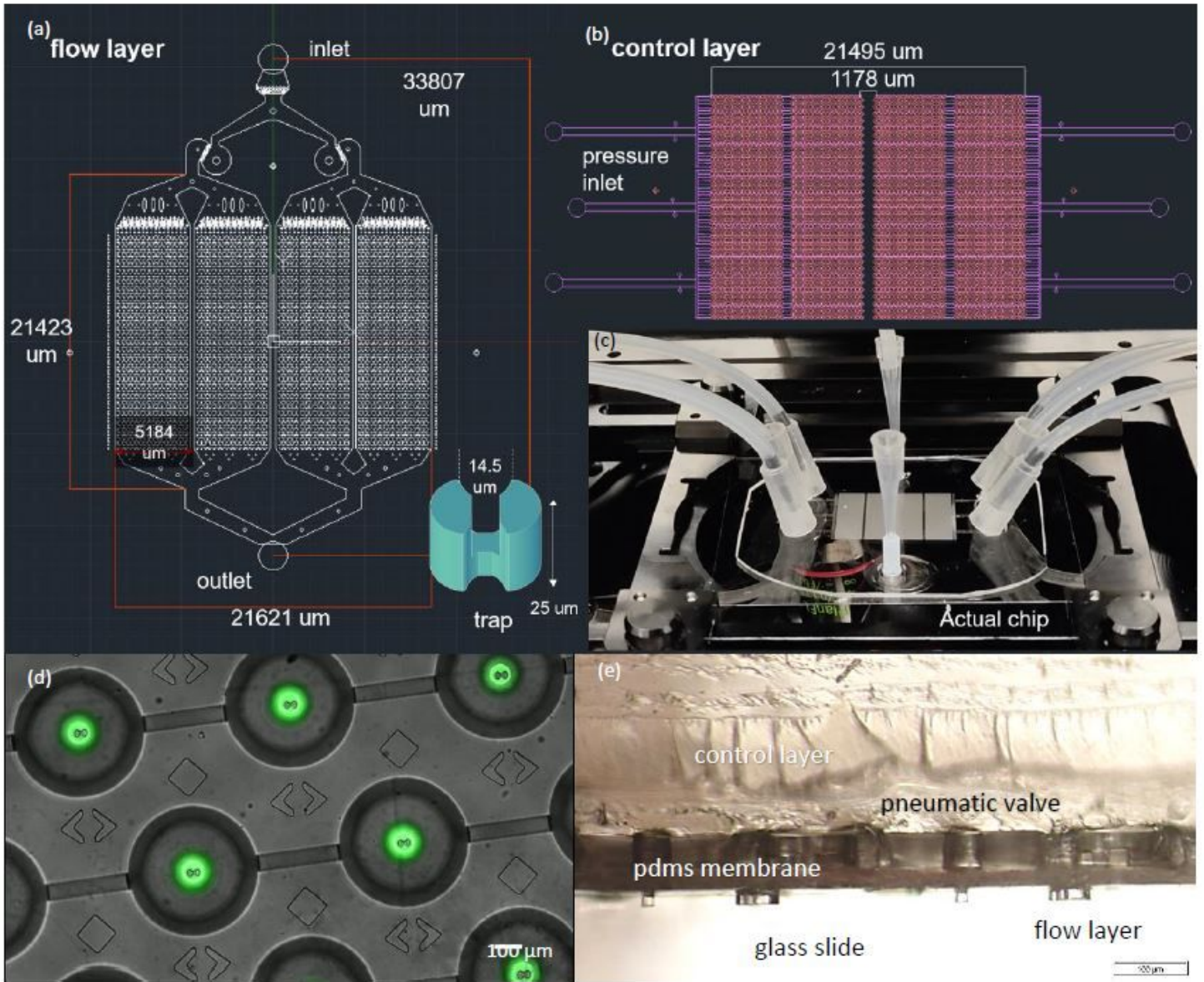


Figure 10

Microfluidic chip design for high throughput single cell assay (a) CAD design of the flow layer (inset) hydrodynamic trap design (b) CAD design of the control layer (c) photo of the assembled microfluidic device (d) microscope image of an array of actuated valves confining a fluorescent solution (e) microscope image of the chip's cross section.

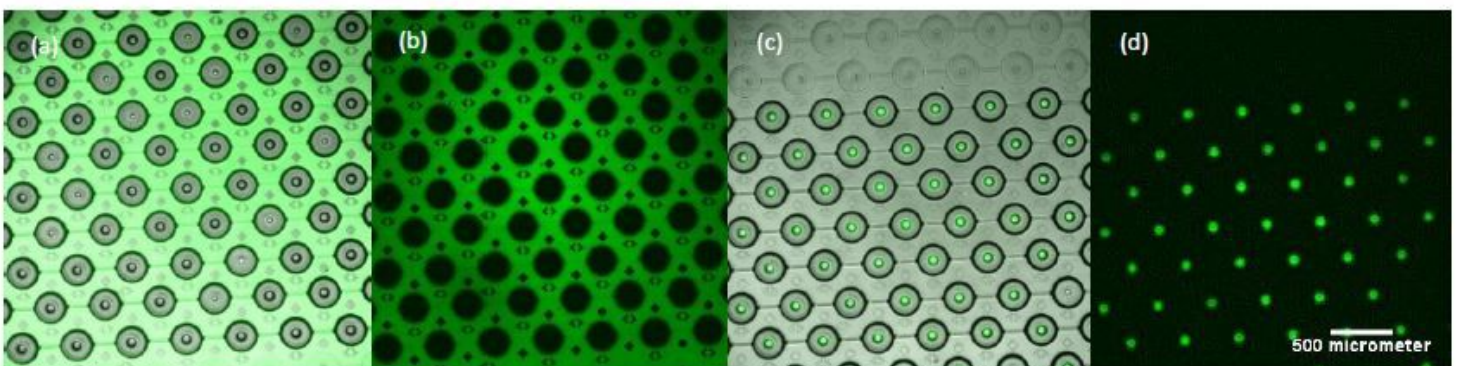


Figure 11

FITC dextran fluorescence solution was used to check the sealing of the microchambers. The solution was made to flow into the channels and the microvalves were actuated (a) multicolor image of the channel and valve array (b) image under FITC (488) filter. After opening-closing the microvalves, the channel was washed by flowing PBS while the valves are actuated leaving the fluorescent solution trap inside the chamber (c) multicolor image (d) image under FITC (488) filter.

Supplementary Files

This is a list of supplementary files associated with this preprint. Click to download.

- [Brionesetalsupplementarymaterial.pdf](#)